# Design of a Transmission-Type Polarization-Insensitive and Angularly Stable Polarization Rotator by Using Characteristic Modes Theory

Francesco Alessio Dicandia, *Member, IEEE*, and Simone Genovesi, *Senior Member, IEEE*

*Abstract*—A novel design strategy for realizing a transmission-type polarization rotator of linearly polarized (LP) plane waves by exploiting the characteristic modes (CMs) theory is described. Design guidelines for the excitation of two current modes on a frequency selective surface (FSS), both exhibiting a circularly polarized (CP) radiated field, are provided to obtain the polarization rotation. The proposed converter exhibits remarkable performance also in the case of oblique incidence and a polarization-insensitive response thanks to the FSS unit cell compactness along with its fourfold rotational symmetry. Specifically, it provides a 3 dB cross-polar transmission percentage bandwidth up to 16.5% with a minimum insertion loss (IL) of 0.1 dB for a normally impinging plane wave whereas in case of an incidence angle of 60° the 3 dB cross-polar transmission percentage bandwidth turns out to be around 14% with a minimum IL of 0.7 dB. Measurements on a realized prototype are in good agreement with simulations, confirming the reliability of the proposed theoretical study.

*Index Terms*—Characteristic modes (CMs), circular polarization, frequency selective surfaces (FSSs), polarization converter.

## I. Introduction

**T**HE manipulation of a plane wave polarization state plays a crucial role in several applications since it is an important feature in many electromagnetic (EM) devices spanning from microwave to optics [1], [2], [3] as well as for future wireless communication systems [4]. One of the most straightforward ways to control the polarization of an EM wave is achieved by resorting to frequency-selective surfaces (FSSs) [5]. Specifically, FSSs consist of periodically arranged subwavelength elements that act as a spatial and frequency filter capable of altering the proprieties of the impinging EM wave, such as transmission and reflection level, phase response, and polarization status [6]. Metasurfaces [7], antennas [8], chipless radio frequency identification (RFID) tags, and sensors [9], [10] represent just some of the applications where

FSSs have been profitably employed. Within this context, they have also found use in devices capable of manipulating the polarization of an EM wave. Among the polarization converters, the rotator represents an interesting subset adopted in imaging radar polarimetry and wireless communication systems [11]. Specifically, a polarization rotator twists the polarization plane of the incident linearly polarized (LP) wave of a predefined angle, usually 90°. Polarization rotators can be grouped into two categories: reflection type and transmission type. The former set [12], [13] requires only the tailoring of the phase response of the grounded reflective surface. Conversely, a transmission rotator needs both amplitude and phase control and therefore it represents a much harder challenge. Over the past years, several polarization transmission rotators were presented. Some of the proposed configurations work at single frequency [14] whereas others present a multiband response [15], [16], [17]. For example, polarization rotators based on substrate-integrated waveguide (SIW) cavities have been reported in [18] and [19]. A bilayer chiral metasurface with the asymmetric transmission is described in [20] whereas an ultrathin polarization rotator based on V-shaped slot FSS is illustrated in [21]. Multilayer structures capable of improving rotation performance have been presented in [22], [23], [24], [25], and [26]. However, they have a not negligible size and a greater susceptibility to manufacturing inaccuracies that may affect the overall reliability and robustness of the design.

Another important class of converters is represented by those who have a polarization-insensitive response [27], [28], [29], [30], [31], meaning that they do not require a stringent alignment between the incident EM wave and the converter. This feature makes these converters suitable to all applicative scenarios where the linear polarization plane of the incident EM wave is unknown or could change over time.

In this framework, one of the most challenging aspects consists of having systematic design guidelines for the synthesis of polarization converters [32]. A theoretical approach to this problem could be provided by the characteristic mode (CM) theory [33]. Indeed, it allows obtaining meaningful insights about scattering and radiation proprieties of the investigated structure, based only on its geometry and shape without considering any excitation source. In the last years, the advantageous exploitation of CM analysis (CMA) has been demonstrated in many applications, including multiple-input multiple-output (MIMO) systems [34], [35], [36], pattern

reconfigurable antennas [37], [38], [39], [40], and metasurfaces [41], [42], [43].

The purpose of this work is to propose a novel strategy for the design of a transmission-type polarization rotator with a polarization-insensitive and angularly stable response. A general and straightforward approach based on the exploitation of the CMA for defining the FSS unit cell is described. Specifically, to enhance the transmission of the incoming LP plane wave, two CMs have been accurately stimulated, each one radiating a circularly polarized (CP) field. It is worth noting that this is the first time that CMA is exploited for the design of a polarization converter and also that it is possible to obtain a CP radiated far-field by exciting a single CM. In fact, so far it has been shown that a CP-radiated field can be obtained by equally stimulating two CMs radiating an LP field and exhibiting a characteristic phase angle difference of 90° [44], [45]. This article is organized as follows. Section II illustrates the required properties of the polarization rotator in terms of its scattered field ($\underline{E}^s$). Section III is devoted to the identification of the polarization rotator unit cell by leveraging the CMA. The performance of the proposed polarization transmission rotator is highlighted in Section IV. Section V is devoted to the manufactured prototype and measurements whereas the conclusions are reported in Section VI.

## II. FEATURES OF THE CONVERTER SCATTERED FIELD

The transmission matrix ($\underline{\underline{\tau}}$) of a transmission-type polarization rotator with a polarization-insensitive response has to be equal to [27]

$$\underline{\underline{\tau}} = \begin{pmatrix} \tau_{xx} & \tau_{xy} \\ \tau_{yx} & \tau_{yy} \end{pmatrix} = e^{j\varphi} \begin{pmatrix} 0 & -1 \\ 1 & 0 \end{pmatrix} \qquad (1)$$

whose element $\tau_{xx}$ ($\tau_{yy}$) refers to the co-polar transmitted component polarized along $x$ ($y$)-axis, $\tau_{xy}$ ($\tau_{yx}$) denotes the cross-polar transmitted component polarized along the $y$ ($x$)-axis by considering an incidence field polarized along the $x$ ($y$) one whereas $\varphi$ represents the phase delay. However, by looking at the transmission matrix it is not clear what conditions the field scattered by the converter ($\underline{E}^s$) must exhibit to satisfy (1). Therefore, a theoretical analysis aimed to derive these radiative characteristics must be carried out. To this end, let us consider an LP EM wave that impinges on a converter based on FSS lying on the $xy$ plane as illustrated in Fig. 1.

A surface current distribution is stimulated on the illuminated scatterer therefore the transmitted electric field ($\underline{E}^t$), propagating along the $z$-axis identified by the unit vector $i_z$, is the result of the superposition of the incident wave ($\underline{E}^i$) and the scattered one ($\underline{E}^s$). The transmitted field has a propagation constant ($\underline{k}^t$), whereas the incident one is equal to ($\underline{k}^i$). For the sake of simplicity, let us consider an orthogonally incident plane wave polarized along the $x$-axis and propagating along $i_z$. In this case, the polarization rotator must be able to generate a scattered field that, once added to incident one, provides a transmitted wave with orthogonal polarization, namely

$$E^i = E_0 i_x; \quad \underline{E}^t = E_0 i_x + \underline{E}^s = e^{j\varphi} E_0 i_y \qquad (2)$$

where $i_x$ and $i_y$ represent the unit vector along the $x$- and $y$-axis, respectively. From (2) it can be inferred that the scattered
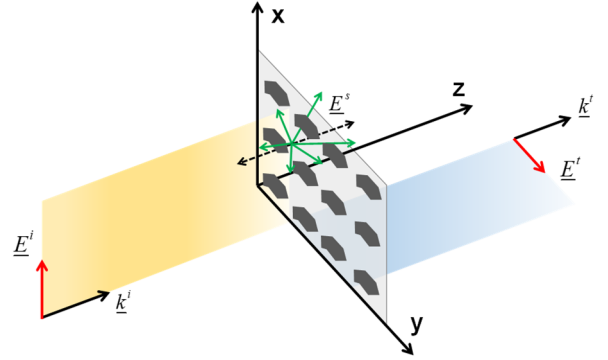


Fig. 1. Schematic of the polarization rotator working principle.

field along $i_z$ has to assume the following general form:

$$\underline{E}^s = -E_0 i_x + e^{j\varphi} E_0 i_y = e^{j\pi}\left(E_0 i_x - e^{j\varphi} E_0 i_y\right). \qquad (3)$$

By looking at (3) the following considerations concerning the scattered field along $i_z$ can be drawn:

1) The scattered field must have both $x$ and $y$ components, namely the same of the incident EM wave and the desired orthogonal one.
2) The scattered component aligned to the incident one must be out-of-phase to it.
3) To ensure a complete transmission the magnitude of the transmitted wave ($|\underline{E}^t|$) must be equal to the magnitude of the incident one ($|\underline{E}^i|$), hence the scattered component propagating along $i_z$ has to guarantee a double power density than the impinging EM wave.

It is worth pointing out that, although the power density scattered field condition the radiated power of the $\underline{E}^s$ is not higher than the incident one. To further develop the analysis and find guidelines for the polarization-rotator design, it is convenient to decompose the LP incident wave as the sum of two CP waves with opposite sense

$$\underline{E}^i = E_0 i_x = \frac{E_0}{2}\left(i_x + j i_y\right) + \frac{E_0}{2}\left(i_x - j i_y\right) \qquad (4)$$

where the first term represents a left-handed CP (LHCP) wave, the second term a right-handed one (RHCP) whereas $E_0$ is the incident wave magnitude ($|\underline{E}^i|$).

By observing (3) and (4) it can be inferred that a straightforward method fulfilling the above scattering conditions on $\underline{E}^s$ is to stimulate the converter with a current distribution that provides a CP wave ($\varphi = \pm 90°$) such as

$$\underline{E}^s = E_s\left(i_x \pm j i_y\right) \qquad (5)$$

where the sign $\pm$ defines the sense (RHCP or LHCP) and $E_s$ is the amplitude of the fields.

Under the assumption that the converter can support a surface current distribution capable of radiating an RHCP scattering field in both axial directions (i.e., $i_z$ and $-i_z$) and a phase delay of 180° with respect to the incident component, the transmitted scattered field along $i_z$ is equal to

$$\underline{E}^{s\_RHCP} = e^{j\pi}\frac{E_0}{2}\left(i_x - j i_y\right) \qquad (6)$$

namely, the RHCP component related to the incident EM wave ($\underline{E}^i$) with the addition of a 180° phase delay. Thereby, the transmitted wave ($\underline{E}^t$) turns out to be

$$\underline{E}^t = \underline{E}^i + \underline{E}^{s\_RHCP} = \frac{E_0}{2}(i_x + ji_y) \tag{7}$$

where it is evident that the transmitted wave ($\underline{E}^t$) appears to be an LHCP wave with a conversion loss of 3 dB. This occurs since the previous power density scattered field conditions are not satisfied and hence half of the power is reflected. For instance, the scattered field (6) with the associated transmitted wave (7), namely a transmission-type linear to circular polarization converter [46], has been attained by employing a CP selective surface (CPSS) [47] and illuminated by an LP impinging plane wave.

Conversely, in case the converter supports an RHCP scattered field only along $i_z$ (i.e., the absence of the back radiation), the transmitted scattered field turns out to be double the RHCP component of the incident wave (4), namely

$$\underline{E}^{s\_RHCP} = e^{j\pi} E_0 (i_x - ji_y). \tag{8}$$

The scattered field in (8) satisfies all the previous requirements necessary to obtain a polarization rotator. By this means, the transmitted wave assumes the following form:

$$\underline{E}^t = E_0 \underline{i}_x + \underline{E}^{s\_RHCP} = jE_0 i_y. \tag{9}$$

Equation (9) proves that a structure capable of generating the scattered field as in (8) yields a 90° polarization rotation without conversion loss.

It is worth noting that, as shown in (3), circular polarization does not represent the only possible solution on $\underline{E}^s$ to achieve a polarization rotator, but in general $\phi$ can be chosen arbitrarily with elliptical polarization. However, since in general CP radiation turns out to be easier to mathematically treat than the elliptical one, CP is recommended.

In the following, the CMA will be used to find a suitable polarization rotator on the basis of the guidelines derived from the described analysis.

## III. CMA OF AN ISOLATED UNIT CELL

With the aim of providing a general and straightforward approach to designing a polarization rotator, the useful insights provided by CMA have been exploited for the identification of the polarization rotator unit cell. Specifically, the first step of the novel design strategy relies on identifying a structure capable of supporting CMs characterized by CP radiation. Next, it is necessary to choose among all the available CMs that, once superimposed, satisfy the desired characteristics on the scattered far-field. Then, it is crucial to verify that the selected set of promising CMs is efficiently stimulated by the incoming LP plane wave.

According to CMA, the total current distribution induced on the investigated structure can be decomposed in terms of linear superposition of orthogonal current modes [33]

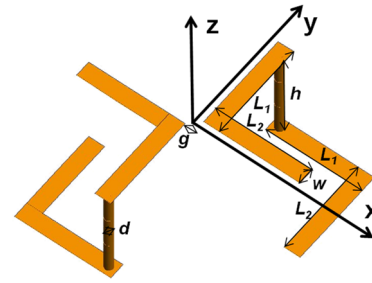$$J_{tot} = \sum_n \frac{V_n}{1 + j\lambda_n} j_n \tag{10}$$



Fig. 2. Two 3-D meandered dipoles with a twofold rotational symmetry layout: $L_1 = 3.94$ mm, $L_2 = 3.94$ mm, $W = 0.65$ mm, $g = 0.4$ mm, $d = 0.35$ mm, and $h = 4.3$ mm.
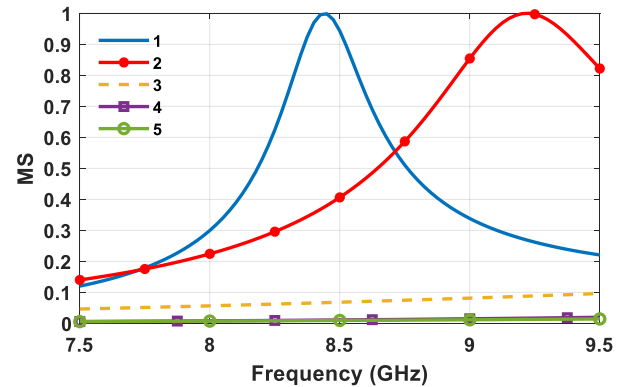


Fig. 3. MS of a 3-D meandered dipole structure with a twofold rotational symmetry.

where $\lambda_n$ is the eigenvalue related to the $n$th current mode $j_n$ whereas $V_n$ represents the excitation capability of the external feeding to stimulate the investigated structure of the $n$th CM. Obviously, in this scenario, the external feeding is represented by the impinging LP wave. Unlike the current modes ($J_n$) distribution and the related $\lambda_n$ that depend only on the geometrical dimensions and shape, the excitation level of a mode ($V_n$) is deeply affected by the polarization and direction of the arrival of the incoming wave.

It is worth noting that the CMA was carried out by characterizing only a single resonator that will be then employed as the unit cell of the periodic structure to realize the final polarization rotator.

### A. Meandered Dipole With Twofold Rotational Symmetry

As stated in Section II, one of the features that the polarization rotator must exhibit is a CP scattered field. One of the most popular structures employed to support a CP scattered field, capable of realizing a CPSS, is based on the Pierrot's cell [48]. Therefore, in the first design step, the CMA of a 3-D meandered dipole shown in Fig. 2 has been carried out.

In particular, the twofold rotational symmetry was employed since it guarantees improved stability with respect to the angle of incidence [49]. Each 3-D dipole of Fig. 2 resembles a Pierrot's cell since it contains two meandered arms connected by a metallic wire.
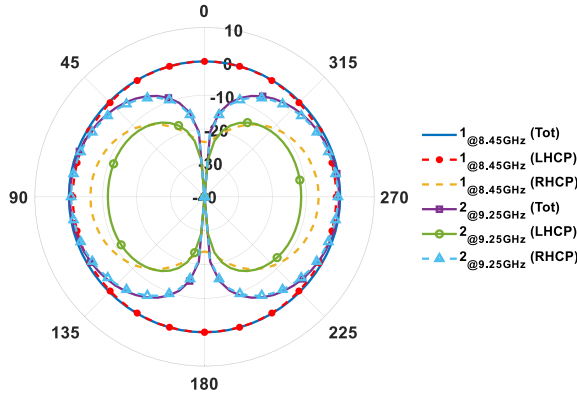
Fig. 4. Normalized modal radiation pattern in dB as a function of $\theta$ angle evaluated at $\phi = 0°$ plane.
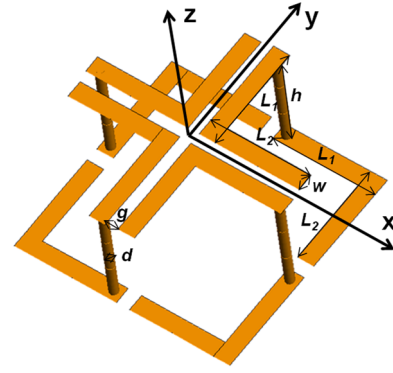


Fig. 5. Four 3-D meandered dipoles with a fourfold rotational symmetry layout: $L_1 = 3.94$ mm, $L_2 = 3.94$ mm, $W = 0.65$ mm, $g = 0.4$ mm, $d = 0.35$ mm, and $h = 4.3$ mm.
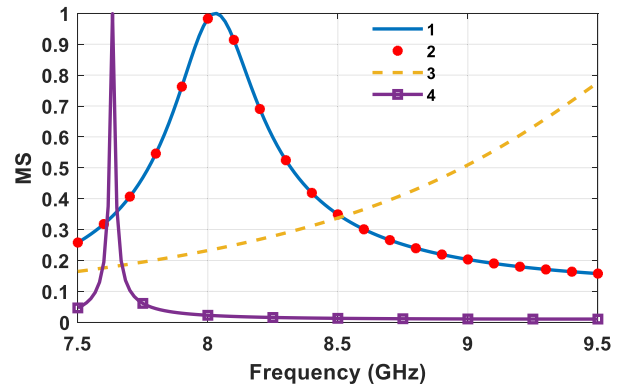


Fig. 6. MS of a 3-D meandered dipole structure with a fourfold rotational symmetry.

The modal significance (MS) of the first five CMs within the 7.5–9.5 GHz frequency bandwidth is reported in Fig. 3. The MS is an important parameter since it describes where a mode is at the resonance (i.e., MS = 1) and its potential contribution to the scattered field ($\underline{E}^s$) [50]. In fact, MS quantifies the modal power contribution to the total radiated power under the assumption it is efficiently excited (i.e., $V_n = 1$). From Fig. 3 it can be drawn that, within the investigated bandwidth, the platform depicted in Fig. 2 supports mainly two modes: Mode 1 with a resonance around 8.45 GHz whereas Mode 2 has a resonance at 9.25 GHz. The other modes hardly give a meaningful radiative contribution due to their low MS value (MS < 0.1). Specifically, at Mode 1 resonance the total length of each meandered dipole turns out to be about $0.53\lambda$, where $\lambda$ is the wavelength at 8.45 GHz.

The normalized modal radiation pattern illustrated in Fig. 4 highlights that Mode 1 presents a bidirectional radiation pattern with a good LHCP radiation purity and a maximum field at $\theta = 0°$ and 180° (i.e., $i_z$ and $-i_z$). Conversely, Mode 2 has an RHCP bidirectional radiation pattern with a pattern null along the broadside direction. Indeed, Mode 2 has a modest MS value and its radiation pattern is unfit for achieving the desired goal.

The CMA emphasized that the 3-D meandered dipole with a twofold rotational symmetry (see Fig. 2) supports a CP CM (Mode 1) with a maximum along both axial directions (i.e., $\theta = 0°$ and 180°), and therefore, it cannot satisfy the unidirectional radiation constraint derived in Section II. Moreover, from the MS of Fig. 2 it can be asserted that around Mode 1 resonance, there is no other CMs that could be suitably stimulated in order to form a combined scattered field capable of satisfying the absence of backscattering radiation.

### B. Meandered Dipole With Fourfold Rotational Symmetry

A step forward for realizing a polarization rotator consists in finding a unit cell structure capable to support multiple CP CMs that are properly stimulated on the platform and are capable to support a CP radiation pattern without backscattering.

The previous CMA suggests a further increase in the number of CMs and a candidate structure is obtained by adding a 90° rotated version of it. Fig. 5 depicts the potential polarization rotator unit cell structure. It comprises four 3-D meandered dipoles arranged with a 90° rotational fourfold symmetry. The MS of the fourfold rotational symmetry layout is shown in Fig. 6. As it is well visible from Fig. 6, the new unit cell supports a pair of CMs, namely Modes 1 and 2, with the same MS behavior (i.e., degenerate modes) with a resonance close to 8 GHz. This modal resonance is mainly determined by the dipole total length (including the vertical wire) that turns out to be about $0.5\lambda$, where $\lambda$ is the wavelength at 8 GHz. The presence of degenerate modes is the first notable difference with respect to the previous 3-D meandered dipole structure with a twofold rotational symmetry (see Fig. 3). Mode 3 can be considered as a high-order mode since its resonance is higher than 9.5 GHz whereas Mode 4 represents a high-quality factor mode with a resonance at 7.63 GHz.

Due to its sharp MS, Mode 4 can be identified as a Fano-type interference [51], which is often exploited in sensor design [52]. Then, with the aim of understanding, if the identified orthogonal CMs can support a CP field, current modes distribution and the related 3-D normalized radiation patterns were investigated and depicted in Figs. 7 and 8, respectively. Modes 1 and 2 exhibit a surface current distribution mainly restricted along two of the four dipoles [see Fig. 7(a) and (b)] whereas Modes 3 and 4 are characterized by a modal
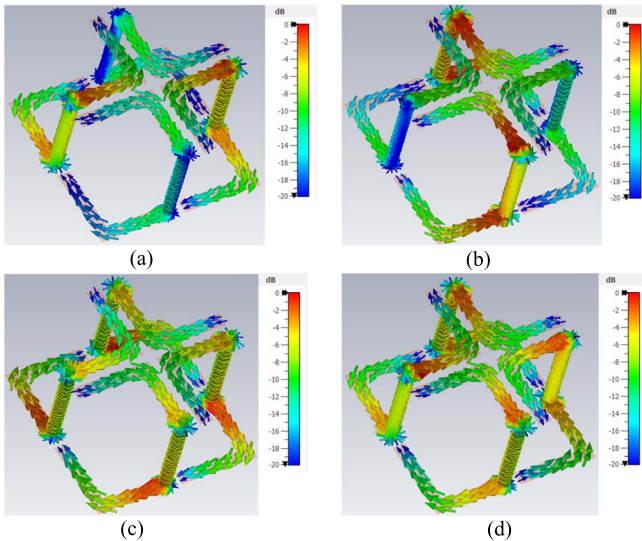
Fig. 7. Normalized current mode distributions in dB on the 3-D meandered dipole structure with a fourfold rotational symmetry related to (a) Mode 1@8 GHz, (b) Mode 2@8 GHz, (c) Mode 3@8 GHz, and (d) Mode 4@7.64 GHz.
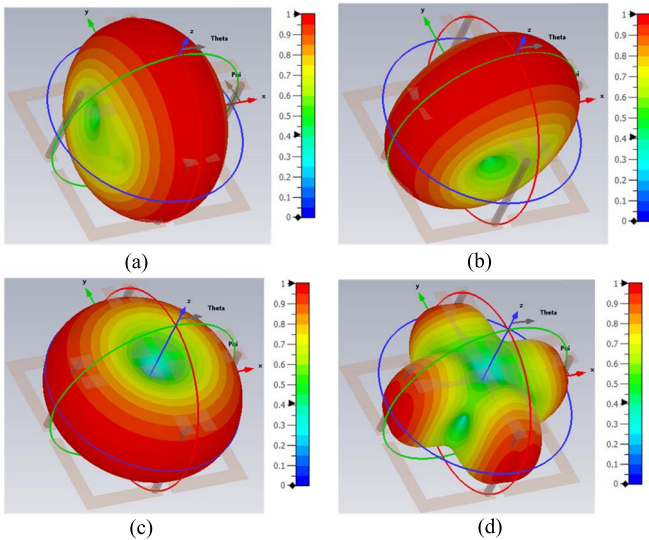


Fig. 8. Normalized mode radiation pattern in linear scale of the 3-D meandered dipole structure with a fourfold rotational symmetry related to (a) Mode 1@8 GHz, (b) Mode 2@8 GHz, (c) Mode 3@8 GHz, and (d) Mode 4@7.64 GHz.

current spread over the entire structure [see Fig. 7(c) and (d)]. Apparently, the first three CMs present a bagel-shaped 3-D radiation pattern [see Fig. 8(a)–(c)]. Specifically, the first two modes present a maximum along $\theta = 0°$ and $180°$ (i.e., $i_z$ and $-i_z$) with a $90°$ phase delay between their modal currents and radiation pattern, whereas Mode 3 is characterized by a pattern null along broadside ($\theta = 0°$). On the contrary, Fano-type interference mode (i.e., Mode 4) exhibits a radiation pattern with four peaks and a pattern null along the broadside direction [see Fig. 8(d)].

By analyzing the MS and the 3-D modal radiation patterns it is possible to conclude that the CMs that could satisfy the derived conditions on the scattered field are Modes 1 and 2.
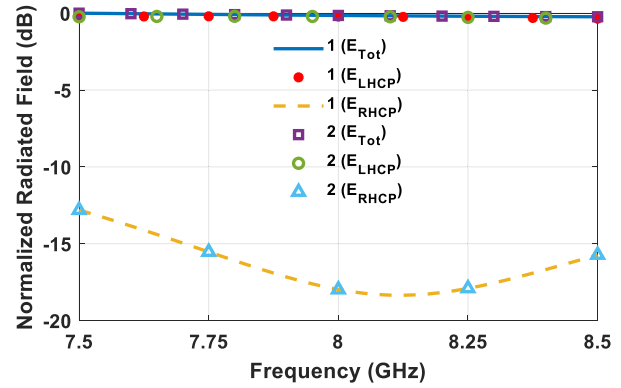


Fig. 9. Normalized radiated field of the first two CMs as a function of the frequency.

The normalized radiated field along the broadside direction is reported as a function of the frequency in Fig. 9 to identify the modal field polarization of the first two modes. By looking at Fig. 9 it is apparent that both the identified CMs radiate mainly an LHCP field with a cross polar component below $-15$ dB from 7.75 to 8.5 GHz. Therefore, the fourfold rotational symmetry structure shown in Fig. 5 allows to double the CP modes number as well as to provides a slight modal resonance reduction (around 6%) with respect to the twofold rotational symmetry (see Fig. 2) due to the coupling among the four dipoles.

Before checking if the identified pair of degenerate CP CMs are capable to satisfy the previous radiative characteristics, it is important to underline that nearby their resonance (i.e., 8 GHz) there is just another CM (i.e., Mode 3) with a modest MS that could give a contribution to the scattered field if stimulated by the incoming LP plane wave. This is an important feature since the fewer undesired CMs are present around the working frequency, the more robust is the platform under oblique incidence. The identification of the desired CMs as well as the undesirable ones represents an interesting feature of the CMA by providing the potential performance of a structure and therefore useful guidelines for the design of the unit cell.

*C. Modal Weighting Coefficient*

The previous CMA investigation emphasized the presence of a couple of CP CMs with a bagel-shaped 3-D radiation pattern in the case of a meandered dipole with fourfold rotational symmetry. However, each CM has a bidirectional radiation pattern, and therefore, as in the case of two 3-D meandered dipoles with a twofold rotational symmetry Mode 1 (see Fig. 2), they cannot satisfy the above-mentioned scattering conditions alone. Therefore, it is necessary to understand if suitable multiple excitations of both Modes 1 and 2 can lead to a CP scattering field with the suppression of the backscattering, which is necessary for realizing an efficient polarization conversion. To this aim, the modal weighting coefficient (MWC), which is the complex amplitude related to each supported mode of (10), has been calculated in the case of a normally impinging LP plane wave with a TM polarization ($\underline{E}^i$ field parallel to the $x$-axis). Fig. 10 highlights that both CP
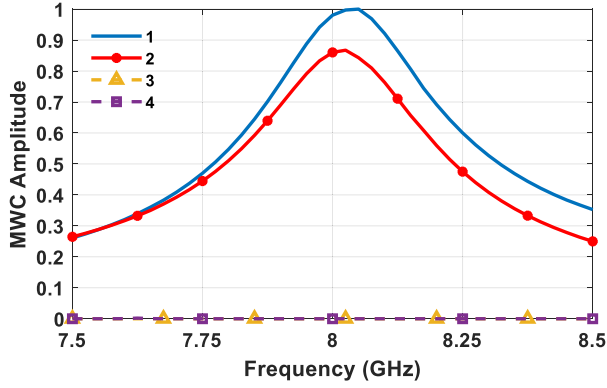
Fig. 10. Normalized MWC amplitude as a function of the frequency in case of normally impinging LP plane wave on the 3-D meandered dipoles with a fourfold rotational symmetry.
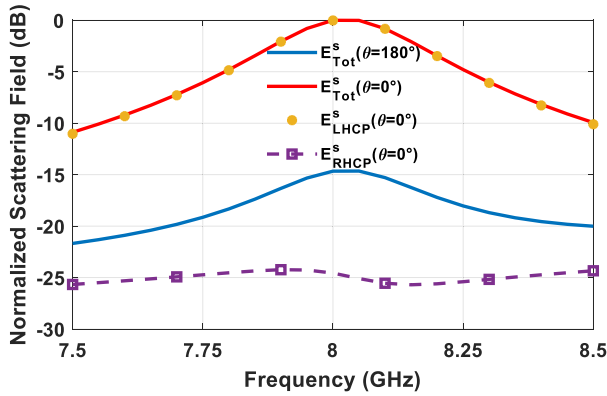


Fig. 11. Normalized scattering field ($E_s$) as a function of the frequency in case of normally impinging LP plane wave on the 3-D meandered dipoles with a fourfold rotational symmetry.

CMs (i.e., Modes 1 and 2), are effectively stimulated by the structure shown in Fig. 5, reaching the maximum stimulation value at their resonance around 8 GHz. The other two CMs are not excited since they have pattern null along broadside direction [see Fig. 8(c) and (d)].

The modal excitation degree of both Modes 1 and 2 lead to the normalized scattered field ($\underline{E}^s$) illustrated in Fig. 11 where it is evident that the investigated platform, under the illumination of a normally impinging LP plane wave, generates an LHCP scattered field with a strong backscattering reduction ($\theta = 180°$). This pivotal feature for obtaining a polarization rotator occurs since a couple of excited CMs has an MWC phase difference close to 90° within the investigated frequency band.

Furthermore, the meandered fourfold-dipole structure has been illuminated with an orthogonally impinging LP plane wave with different azimuth angles ($\phi_i = 0°$, 22.5°, 45°, 67.5°, and 90°) and the normalized MWC amplitude has been reported in Fig. 12.

It can be seen that the proposed platform is capable of efficiently supporting both Modes 1 and 2, regardless of the electric field orientation. All the other modes continue to be unexcited due to their modal pattern null along the broadside [see Fig. 8(c) and (d)]. Specifically, the MWC amplitude of
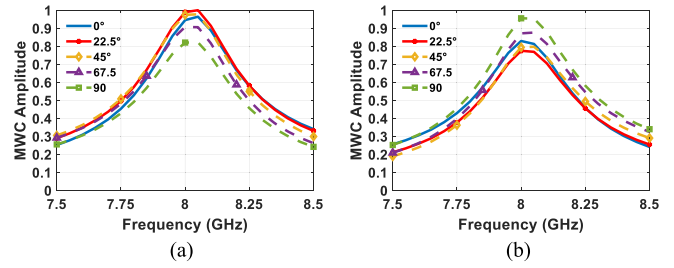


Fig. 12. Normalized MWC amplitude as a function of the impinging LP plane wave polarization ($\phi_i$) on the 3-D meandered dipoles with a fourfold rotational symmetry: (a) Mode 1 and (b) Mode 2.
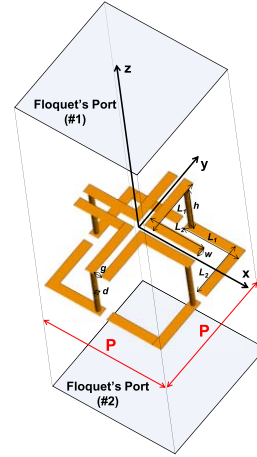


Fig. 13. Simulation setup of the proposed polarization converter unit cell.

Mode 1 [see Fig. 12(a)] slightly increases by altering the azimuth angle ($\varphi_i$) from 0° to 22.5° then it fades little by little. The MWC amplitude of Mode 2 [see Fig. 12(b)] presents the same behavior but with an opposite trend. This fact is on the basis of the polarization-insensitive capability of the proposed platform since the normalized scattered field remains the same (see Fig. 11) for any polarization orientation of the incoming LP wave.

The CMA has confirmed that the investigated unit cell satisfies the necessary requirements and hence the proposed 3-D meandered dipoles arranged with a 90° rotational fourfold symmetry can be profitably adopted in a polarization rotator.

## IV. POLARIZATION TRANSMISSION ROTATOR

The structure designed with the help of the CMA has then been employed as the unit cell of an FSS to finally assess its polarization conversion capability. Regarding the FSS periodicity ($P$), generally, it should be less than half of the wavelength for avoiding the grating lobes onset in case of oblique incidence. Therefore, it is favorable to keep it as small as possible to be less sensitive to large incidence angles as well as to increase the working bandwidth [53]. The considered periodicity has been set equal to $P = 9.2$ mm (see Fig. 13) and a full-wave simulation has been carried out with CST Microwave Studio.

The frequency response in terms of co-polar ($\tau_{co}$) and cross-polar ($\tau_{cross}$) transmission coefficients for different LP
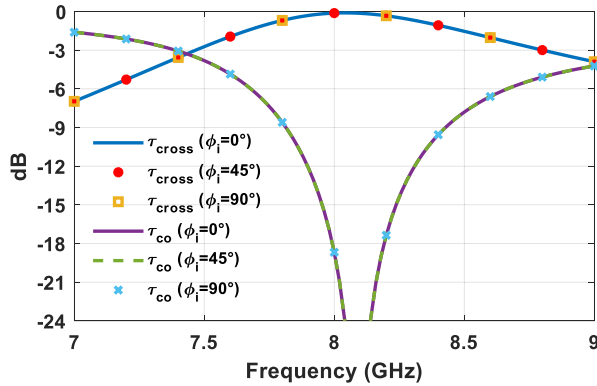
Fig. 14. Co-polar ($\tau_{co}$) and cross-polar ($\tau_{cross}$) transmission coefficient in dB as a function of frequency for different normally incidence LP plane wave polarizations ($\phi_i$).



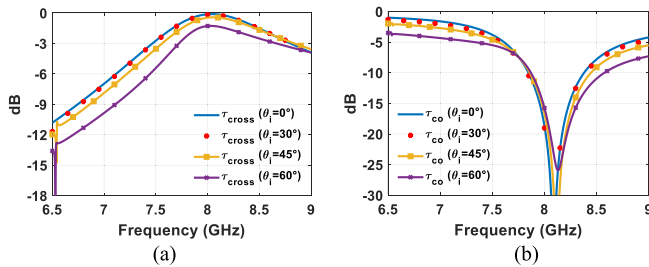Fig. 15. (a) Cross-polar ($\tau_{cross}$) and (b) co-polar ($\tau_{co}$) transmission coefficient in dB as a function of frequency for different LP plane wave incidence angles ($\theta_i$) evaluated in the xz plane for TE illumination.
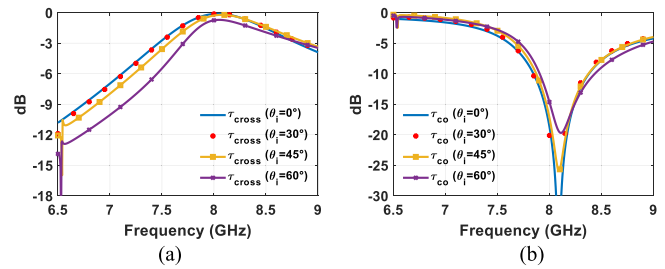


Fig. 16. (a) Cross-polar ($\tau_{cross}$) and (b) co-polar ($\tau_{co}$) transmission coefficient in dB as a function of frequency for different LP plane wave incidence angles ($\theta_i$) evaluated in the xz plane for TM illumination.
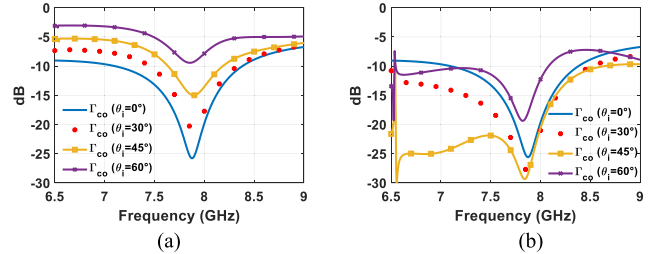


Fig. 17. Co-polar reflection coefficient ($\Gamma_{co}$) in dB as a function of frequency for different LP plane wave incidence angles ($\theta_i$) evaluated in the xz plane in case of (a) TE and (b) TM illumination.

TABLE I
ANGULAR STABILITY OF THE PROPOSED POLARIZER

|  | Illumination | $BW_{-3dB}$ (%) | Range (GHz) | min IL (dB) |
|---|---|---|---|---|
| $\theta_i = 0°$ | TE/TM | 16.5 | 7.46-8.8 | 0.11 |
| $\theta_i = 30°$ | TE | 16.35 | 7.47-8.8 | 0.17 |
|  | TM | 16.9 | 7.46-8.84 | 0.11 |
| $\theta_i = 45°$ | TE | 15.63 | 7.55-8.83 | 0.42 |
|  | TM | 16.28 | 7.56-8.9 | 0.21 |
| $\theta_i = 60°$ | TE | 11.6 | 7.72-8.67 | 1.27 |
|  | TM | 13.8 | 7.7-8.84 | 0.71 |

plane wave polarization ($\phi_i$) is reported in Fig. 14 for normal incidence.

The frequency response confirms the previous CMA results. Indeed, the FSS converter based on the proposed unit cell realizes a polarization rotation of the impinging wave operating at around 8 GHz with a minimum $\tau_{cross}$ of $-0.11$ dB and a percentage bandwidth ($BW_{-3\,dB}$) equal to 16.5%, defined as the frequency range within which $\tau_{cross}$ turns out to be higher than $-3$ dB. Moreover, since all the curves of Fig. 14 are fully overlapped for all the incoming LP plane wave polarizations ($\phi_i$), the investigated polarization converter appears to be independent of the orientation of the impinging LP plane wave, by confirming the polarization insensitive feature of the proposed structure. This occurs due to the efficient excitation on the proposed unit cell platform of both CP CMs (i.e., Modes 1 and 2), as accurately predicted by the CMA.

Afterward, the investigated FSS has been analyzed under various LP plane wave incidence angles ($\theta_i$) in the range of 0°–60° for both the TE and TM illumination in the xz plane ($\phi = 0°$), with the purpose of examining the polarization-conversion robustness (see Figs. 15 and 16).

From Figs. 15 and 16 it can be drawn that the frequency response remains stable up to $\theta_i = 30°$, after that the rotator response undergoes a mild worsening, especially for $\theta_i = 60°$ and TE illumination (see Fig. 15) where the converter suffers a slight working bandwidth reduction as well as a higher minimum cross-polar ($\tau_{cross}$) transmission loss (1.27 dB). In addition, the co-polar reflection coefficient ($\Gamma_{co}$) as a

function of the frequency for both the TE and TM illumination in the xz plane ($\phi = 0°$) has been shown in Fig. 17.

Table I reports some interesting information regarding angular stability in terms of cross-polar transmission percentage bandwidth ($BW_{-3\,dB}$), working frequency range, and minimum insertion loss (IL) within the working bandwidth. It is evident that with the increasing of the incidence angle ($\theta_i$) there is a small percentage $BW_{-3\,dB}$ reduction, passing from 16.5% for normal incidence to 13.8% in the case of $\theta_i = 60°$ with TM incidence (11.6% for TE immunization). The $BW_{-3\,dB}$ drop is due to the increase in the minimum working frequency range. Likewise, the greater the LP plane wave incidence angle ($\theta_i$), the higher the minimum IL within the bandwidth. All in all, the proposed converter exhibits remarkable angular stability, especially for TM illumination.

Additionally, by looking at both Figs. 15 and 16, it is interesting to remark on a sharp distortion of the cross-polar ($\tau_{cross}$) transmission coefficient at around 6.5 GHz in the case

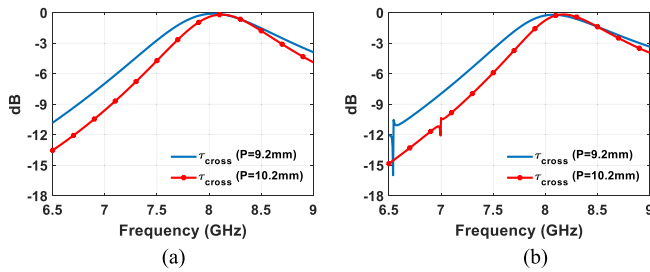Fig. 18. Cross-polar ($\tau_{cross}$) transmission coefficient in dB as a function of frequency in the $xz$ plane and TM illumination for two different unit cell periodicities ($P$) in case of (a) normally and (b) $\theta_i = 45°$ incidence angle.



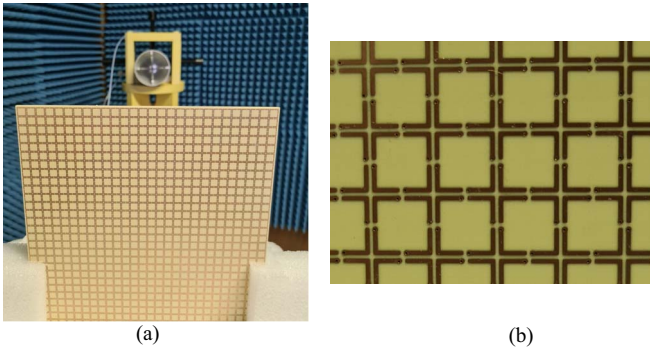Fig. 20. Comparison between simulated and measured (a) cross-polar ($\tau_{cross}$) and (b) co-polar ($\tau_{co}$) transmission coefficient in dB as a function of frequency for a normally incident LP plane wave with a polarization angle ($\varphi_i$) of 0°, 45°, and 90°.



Fig. 19. (a) Polarization transmission rotator manufactured prototype and (b) zoom view of some unit cells.



Fig. 21. Comparison between simulated and measured cross-polar ($\tau_{cross}$) transmission coefficient in dB as a function of frequency for different LP plane wave incidence angles ($\theta_i$) evaluated in the $xz$ plane in case of (a) TE and (b) TM illumination.

of oblique incidence. This phenomenon is due to the excitation on the converter unit cells of the Fano-type interference CM, previously identified in the CMA as Mode 4. It is interesting that the CMA on the isolated element detected the Fano interference CM with a resonance at 7.63 GHz (see Fig. 6) and not at around 6.5 GHz as illustrated in Figs. 15 and 16. In fact, the resonance frequency of the fundamental CP CMs (i.e., Modes 1 and 2), which are responsible for the polarization conversion, is not shifted, whereas the Fano interference observed in the CMA turns out to be much more altered. This could be due to a greater effect of the coupling with the neighboring cells experienced by the Fano resonance with respect to the fundamental ones. To prove this, the cross-polar ($\tau_{cross}$) transmission coefficient for two different unit cell periodicities ($P$) has been investigated and reported in Fig. 18.

From Fig. 18 it is well visible that, in the case of $P = 9.2$ mm the Fano resonance occurs at around 6.5 GHz whereas it reaches 7 GHz when the periodicity becomes $P = 10.2$ mm, approaching 7.63 GHz detected in the isolated scenario through CMA. Summarizing, the converter central working frequency observed in the isolated unit cell turns out to be stable and not dependent on the adopted periodicity whereas reduction of it determines a significant decrease of the Fano resonance.

## V. PROTOTYPE AND MEASUREMENTS

A prototype based on 28 × 28 unit cells has been manufactured to assess the reliability of the proposed polarization converter designed with the CMA support. The whole fabricated
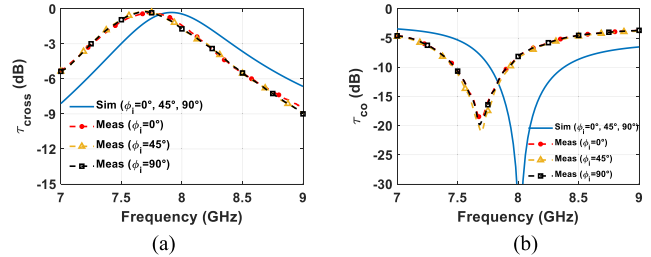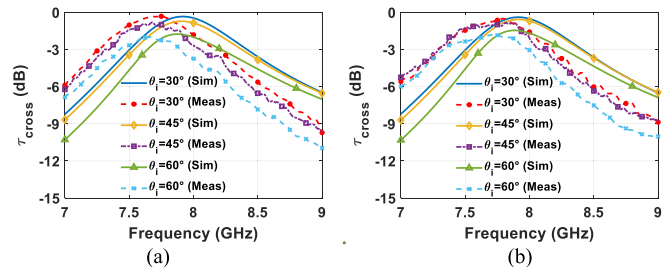
prototype and a zoomed-in view of a few unit cells are shown in Fig. 19. As a proof of concept, the proposed polarization transmission rotator has been etched on a dielectric substrate layer (ISOLA IS680-280, $\varepsilon_r = 2.8$, $\tan\delta = 0.0025$) with a thickness of 3.04 mm ($0.08\lambda_{@8\ GHz}$). The converter geometrical dimensions have been slightly retuned with respect to the previous section owing to the presence of the dielectric layer whereas the diameter of the metallic through-holes is 0.3 mm.

The performance of the fabricated converter has been assessed by placing it in between two dual-polarized horn antennas (MVG QR2000, 2–18 GHz) connected to a four ports vector network analyzer (Anritsu Shockline MS46524B). The polarizer and the antennas are separated by more than 1 m.

The measured cross-polar ($\tau_{cross}$) and co-polar ($\tau_{co}$) transmission coefficient as a function of frequency for different normally impinging LP polarizations ($\varphi_i$) is shown in Fig. 20.

The agreement with the simulated values is satisfactory although the measured ones are characterized by a slight frequency downshift. This is probably due to fabrication tolerance as well as a mild variation of the dielectric substrate thickness or dielectric constant with respect to the simulated ones. From Fig. 20 it can be seen that, for a normally impinging LP wave, the measured percentage bandwidth ($BW_{-3\ dB}$) is around 12.3% (7.25–8.2 GHz) with a minimum $\tau_{cross}$ of $-0.32$ dB independently of the impinging LP plane wave orientation.

The comparison between simulated and measured $\tau_{cross}$ transmission coefficient as a function of frequency in the case of oblique incidence is reported in Fig. 21. It can be drawn that with the increasing of incidence angle ($\theta_i$) occurs

<div align="center">TABLE II</div>
<div align="center">MEASURED PERFORMANCE COMPARISON AMONG DIFFERENT TRANSMISSION-TYPE POLARIZATION INSENSITIVE ROTATORS</div>

| Ref. | Metallic Layers | Dielectric Layers | Incidence Angle (deg) | $BW_{-3dB}$ (%) | min IL (dB) |
|---|---|---|---|---|---|
| [27] | 3 | 2 ($\varepsilon_r$=2.65) | 0 | 12 | 0.16 |
| [28] | 2 | 1 ($\varepsilon_r$=2.2) | 0 | 5.5 | 0.2 |
| [29] | 2 | 1 ($\varepsilon_r$=3.5) | 0 | 6.5 | 0.5 |
| [30] | 3 | 2 ($\varepsilon_r$=2.1) | 0 | 4.3 | 0.04 |
| This work | 2 | 1 ($\varepsilon_r$=2.8) | 0 | 12.3 | 0.32 |
| | | | 60 | 8.5 | 1.8 |

a $BW_{-3\,dB}$ shrinking for both the TE and TM polarization. Specifically, the measured TE $\tau_{cross}$ transmission coefficient [see Fig. 21(a)] provides a $BW_{-3\,dB}$ of 11.9%, 9.6%, and 6.2% by considering an incidence angle of 30°, 45°, and 60°, respectively. Conversely, the measured TM one guarantees a $BW_{-3\,dB}$ of 11.5%, 10.8%, and 8.5%. Moreover, the higher the incidence angle the lower the minimum $\tau_{cross}$ transmission coefficient. Specifically, by considering an incidence angle from 30° to 60°, the measured minimum $\tau_{cross}$ in the case of TE polarization is between −0.4 and −1.98 dB whereas the TM one range is from −0.5 to −1.8 dB.

Therefore, as remarked in the previous section (see Table I), the TM polarization highlights a more robust frequency response with respect to the oblique incidence. It is worth remarking that, higher-quality materials and manufacturing processes such as the employment of a foam substrate layer [54], would make it possible to get closer to the theoretical performance highlighted in Section IV.

The performance of the proposed polarization insensitive converter is summarized in Table II and compared with those of other solutions in terms of the number of metallic and dielectric layers, 3 dB cross polar transmission bandwidth ($BW_{-3\,dB}$), and minimum IL. It is apparent that the proposed polarization converter outperforms all the structures with two metallic layers both in terms of $BW_{-3\,dB}$ and angular stability. Moreover, the proposed converter offers better performance [30] or comparable $BW_{-3\,dB}$ [27] with respect to structures requiring three metallic layers and two dielectric substrates.

## VI. CONCLUSION

An innovative design strategy has been proposed for designing a polarization converter by resorting to the CMA. The conditions to be satisfied by the polarization rotator have been individuated in terms of the scattered field properties. Then, the CMA has been exploited to find a proper unit cell exhibiting a scattered field able to satisfy the imposed requirements. The CMA insight provided design guidelines for the suitable excitation of two CP CMs in order to obtain a polarization transmission rotator with low IL and a polarization-insensitive response. The results showed a remarkable performance combining wide 3 dB percentage bandwidth, low minimum IL, and

significant robustness with respect to the oblique incidence by exploiting the FSS unit cell compactness. As proof of concept, a prototype has been manufactured to assess the reliability of the proposed strategy. The measured and simulated results present a good agreement and confirm the feasibility of the described design process based on the fruitful exploitation of CMA.

## REFERENCES

[1] J. Hao et al., "Manipulating electromagnetic wave polarizations by anisotropic metamaterials," *Phys. Rev. Lett.*, vol. 99, Aug. 2007, Art. no. 063908, doi: 10.1103/PhysRevLett.99.063908.

[2] M. Eular, V. Fusco, R. Cahill, and R. Dickie, "325 GHz single layer sub-millimeter wave FSS based split slot ring linear to circular polarization convertor," *IEEE Trans. Antennas Propag.*, vol. 58, no. 7, pp. 2457–2459, Jul. 2010, doi: 10.1109/TAP.2010.2048874.

[3] W. Sun, Q. He, J. Hao, and L. Zhou, "A transparent metamaterial to manipulate electromagnetic wave polarizations," *Opt. Lett.*, vol. 36, no. 6, p. 927, Mar. 2011, doi: 10.1364/OL.36.000927.

[4] F. A. Dicandia, N. J. G. Fonseca, M. Bacco, S. Mugnaini, and S. Genovesi, "Space-air-ground integrated 6G wireless communication networks: A review of antenna technologies and application scenarios," *Sensors*, vol. 22, no. 9, p. 3136, Apr. 2022, doi: 10.3390/s22093136.

[5] V. S. Asadchy, A. Díaz-Rubio, and S. A. Tretyakov, "Bianisotropic metasurfaces: Physics and applications," *Nanophotonics*, vol. 7, no. 6, pp. 1069–1094, 2018, doi: 10.1515/nanoph-2017-0132.

[6] S. B. Glybovski, S. A. Tretyakov, P. A. Belov, Y. S. Kivshar, and C. R. Simovski, "Metasurfaces: From microwaves to visible," *Phys. Rep.*, vol. 634, pp. 1–72, Apr. 2016, doi: 10.1016/j.physrep.2016.04.004.

[7] C. L. Holloway, E. F. Kuester, J. A. Gordon, J. O'Hara, J. Booth, and D. R. Smith, "An overview of the theory and applications of metasurfaces: The two-dimensional equivalents of metamaterials," *IEEE Antennas Propag. Mag.*, vol. 54, no. 2, pp. 10–35, Apr. 2012, doi: 10.1109/MAP.2012.6230714.

[8] M. Faenzi et al., "Metasurface antennas: New models, applications and realizations," *Sci. Rep.*, vol. 9, no. 1, 2019, Art. no. 10178, doi: 10.1038/s41598-019-46522-z.

[9] S. Genovesi, F. Costa, F. A. Dicandia, M. Borgese, and G. Manara, "Orientation-insensitive and normalization-free reading chipless RFID system based on circular polarization interrogation," *IEEE Trans. Antennas Propag.*, vol. 68, no. 3, pp. 2370–2378, Mar. 2020, doi: 10.1109/TAP.2019.2949417.

[10] S. Genovesi, F. Costa, M. Borgese, F. Dicandia, and G. Manara, "Chipless radio frequency identification (RFID) sensor for angular rotation monitoring," *Technologies*, vol. 6, no. 3, p. 61, Jun. 2018, doi: 10.3390/technologies6030061.

[11] H. A. Zebker and J. J. Van Zyl, "Imaging radar polarimetry: A review," *Proc. IEEE*, vol. 79, no. 11, pp. 1583–1606, Nov. 1991, doi: 10.1109/5.118982.

[12] W. Yang, K. W. Tam, W. W. Choi, W. Che, and H. T. Hui, "Novel polarization rotation technique based on an artificial magnetic conductor and its application in a low-profile circular polarization antenna," *IEEE Trans. Antennas Propag.*, vol. 62, no. 12, pp. 6206–6216, Dec. 2014, doi: 10.1109/TAP.2014.2361130.

[13] X. Gao, X. Han, W.-P. Cao, H. O. Li, H. F. Ma, and T. J. Cui, "Ultrawideband and high-efficiency linear polarization converter based on double V-shaped metasurface," *IEEE Trans. Antennas Propag.*, vol. 63, no. 8, pp. 3522–3530, Aug. 2015, doi: 10.1109/TAP.2015.2434392.

[14] T. Niemi, A. O. Karilainen, and S. A. Tretyakov, "Synthesis of polarization transformers," *IEEE Trans. Antennas Propag.*, vol. 61, no. 6, pp. 3102–3111, Jun. 2013, doi: 10.1109/TAP.2013.2252136.

[15] Y. Cheng, W. Li, and X. Mao, "Triple-band polarization angle independent 90° polarization rotator based on Fermat's spiral structure planar chiral metamaterial," *Prog. Electromagn. Res.*, vol. 165, pp. 35–45, 2019, doi: 10.2528/PIER18112603.

[16] S.-Y. Wang, W. Liu, and W. Geyi, "Dual-band transmission polarization converter based on planar-dipole pair frequency selective surface," *Sci. Rep.*, vol. 8, no. 1, p. 3791, Dec. 2018, doi: 10.1038/s41598-018-22092-4.

[17] D. J. Liu, Z. Y. Xiao, and Z. H. Wang, "Multi-band asymmetric transmission and 90° polarization rotator based on bi-layered metasurface with F-shaped structure," *Plasmonics*, vol. 12, no. 2, pp. 445–452, Apr. 2017, doi: 10.1007/s11468-016-0284-4.

[18] E. Arnieri, F. Greco, L. Boccia, and G. Amendola, "A SIW-based polarization rotator with an application to linear-to-circular dual-band polarizers at K-/Ka-band," *IEEE Trans. Antennas Propag.*, vol. 68, no. 5, pp. 3730–3738, May 2020, doi: 10.1109/TAP.2020.2963901.

[19] S. A. Winkler, W. Hong, M. Bozzi, and K. Wu, "Polarization rotating frequency selective surface based on substrate integrated waveguide technology," *IEEE Trans. Antennas Propag.*, vol. 58, no. 4, pp. 1202–1213, Apr. 2010, doi: 10.1109/TAP.2010.2041170.

[20] S. H. A. Bokhari and H. M. Cheema, "A bilayered, broadband, angularly robust chiral metasurface for asymmetric transmission," *IEEE Antennas Wireless Propag. Lett.*, vol. 20, no. 1, pp. 23–27, Jan. 2021, doi: 10.1109/LAWP.2020.3037045.

[21] M. Saikia, S. Ghosh, and K. V. Srivastava, "Design and analysis of ultrathin polarization rotating frequency selective surface using V-shaped slots," *IEEE Antennas Wireless Propag. Lett.*, vol. 16, pp. 2022–2025, 2017, doi: 10.1109/LAWP.2017.2693685.

[22] J.-M. Xie, B. Li, L. Zhu, and H. Li, "High-order bandpass polarization rotator based on aperture-coupled patch resonators," *IEEE Antennas Wireless Propag. Lett.*, vol. 20, no. 9, pp. 1809–1813, Sep. 2021, doi: 10.1109/LAWP.2021.3097413.

[23] A. A. Omar, Z. Shen, and S. Y. Ho, "Multiband and wideband 90° polarization rotators," *IEEE Antennas Wireless Propag. Lett.*, vol. 17, no. 10, pp. 1822–1826, Oct. 2018, doi: 10.1109/LAWP.2018.2867489.

[24] L. Li, Y. Li, Z. Wu, F. Huo, Y. Zhang, and C. Zhao, "Novel polarization-reconfigurable converter based on multilayer frequency-selective surfaces," *Proc. IEEE*, vol. 103, no. 7, pp. 1057–1070, Jul. 2015, doi: 10.1109/JPROC.2015.2437611.

[25] F. Costa and M. Borgese, "Systematic design of transmission-type polarization converters comprising multilayered anisotropic metasurfaces," *Phys. Rev. A, Gen. Phys.*, vol. 14, no. 3, Sep. 2020, Art. no. 034049, doi: 10.1103/PhysRevApplied.14.034049.

[26] T.-K. Wu, "Meander-line polarizer for arbitrary rotation of linear polarization," *IEEE Microw. Guided Wave Lett.*, vol. 4, no. 6, pp. 199–201, Jun. 1994, doi: 10.1109/75.294292.

[27] S.-Y. Wang, J.-D. Bi, W. Liu, W. Geyi, and S. Gao, "Polarization-insensitive cross-polarization converter," *IEEE Trans. Antennas Propag.*, vol. 69, no. 8, pp. 4670–4680, Aug. 2021, doi: 10.1109/TAP.2021.3060087.

[28] Y. Ye and S. He, "90° polarization rotator using a bilayered chiral metamaterial with giant optical activity," *Appl. Phys. Lett.*, vol. 96, no. 20, May 2010, Art. no. 203501, doi: 10.1063/1.3429683.

[29] H. Shi, A. Zhang, S. Zheng, J. Li, and Y. Jiang, "Dual-band polarization angle independent 90° polarization rotator using twisted electric-field-coupled resonators," *Appl. Phys. Lett.*, vol. 104, no. 3, Jan. 2014, Art. no. 034102, doi: 10.1063/1.4863227.

[30] M. Mutlu and E. Ozbay, "A transparent 90° polarization rotator by combining chirality and electromagnetic wave tunneling," *Appl. Phys. Lett.*, vol. 100, no. 5, Jan. 2012, Art. no. 051909, doi: 10.1063/1.3682591.

[31] H. S. Park, T.-T. Kim, H.-D. Kim, K. Kim, and B. Min, "Nondispersive optical activity of meshed helical metamaterials," *Nature Commun.*, vol. 5, no. 1, p. 5435, Dec. 2014, doi: 10.1038/ncomms6435.

[32] X. You, C. Fumeaux, and W. Withayachumnankul, "Tutorial on broadband transmissive metasurfaces for wavefront and polarization control of terahertz waves," *J. Appl. Phys.*, vol. 131, no. 6, Feb. 2022, Art. no. 061101, doi: 10.1063/5.0077652.

[33] R. F. Harrington and J. R. Mautz, "Theory of characteristic modes for conducting bodies," *IEEE Trans. Antennas Propag.*, vol. AP-19, no. 5, pp. 622–628, Sep. 1971, doi: 10.1109/TAP.1971.1139999.

[34] C. Deng, Z. Feng, and S. V. Hum, "MIMO mobile handset antenna merging characteristic modes for increased bandwidth," *IEEE Trans. Antennas Propag.*, vol. 64, no. 7, pp. 2660–2667, Jul. 2016, doi: 10.1109/TAP.2016.2537358.

[35] D. Manteuffel and R. Martens, "Compact multimode multielement antenna for indoor UWB massive MIMO," *IEEE Trans. Antennas Propag.*, vol. 64, no. 7, pp. 2689–2697, Jul. 2016, doi: 10.1109/TAP.2016.2537388.

[36] H. Li, Z. T. Miers, and B. K. Lau, "Design of orthogonal MIMO handset antennas based on characteristic mode manipulation at frequency bands below 1 GHz," *IEEE Trans. Antennas Propag.*, vol. 62, no. 5, pp. 2756–2766, May 2014, doi: 10.1109/TAP.2014.2308530.

[37] F. A. Dicandia, S. Genovesi, and A. Monorchio, "Null-steering antenna design using phase-shifted characteristic modes," *IEEE Trans. Antennas Propag.*, vol. 64, no. 7, pp. 2698–2706, Jul. 2016, doi: 10.1109/TAP.2016.2556700.

[38] F. A. Dicandia, S. Genovesi, and A. Monorchio, "Advantageous exploitation of characteristic modes analysis for the design of 3-D null-scanning antennas," *IEEE Trans. Antennas Propag.*, vol. 65, no. 8, pp. 3924–3934, Aug. 2017, doi: 10.1109/TAP.2017.2716402.

[39] F. A. Dicandia, S. Genovesi, and A. Monorchio, "Efficient excitation of characteristic modes for radiation pattern control by using a novel balanced inductive coupling element," *IEEE Trans. Antennas Propag.*, vol. 66, no. 3, pp. 1102–1113, Mar. 2018, doi: 10.1109/TAP.2018.2790046.

[40] F. A. Dicandia and S. Genovesi, "A compact cubeSat antenna with beamsteering capability and polarization agility: Characteristic modes theory for breakthrough antenna design," *IEEE Antennas Propag. Mag.*, vol. 62, no. 4, pp. 82–93, Aug. 2020, doi: 10.1109/MAP.2020.2965015.

[41] T. Li et al., "Characteristic mode inspired dual-polarized double-layer metasurface lens," *IEEE Trans. Antennas Propag.*, vol. 69, no. 6, pp. 3144–3154, Jun. 2021, doi: 10.1109/TAP.2020.3046423.

[42] F. H. Lin and Z. N. Chen, "Low-profile wideband metasurface antennas using characteristic mode analysis," *IEEE Trans. Antennas Propag.*, vol. 65, no. 4, pp. 1706–1713, Apr. 2017, doi: 10.1109/TAP.2017.2671036.

[43] F. A. Dicandia and S. Genovesi, "Characteristic modes analysis of non-uniform metasurface superstrate for nanosatellite antenna design," *IEEE Access*, vol. 8, pp. 176050–176061, 2020, doi: 10.1109/ACCESS.2020.3027251.

[44] J. Zeng, X. Liang, L. He, F. Guan, F. H. Lin, and J. Zi, "Single-fed triple-mode wideband circularly polarized microstrip antennas using characteristic mode analysis," *IEEE Trans. Antennas Propag.*, vol. 70, no. 2, pp. 846–855, Feb. 2022, doi: 10.1109/TAP.2021.3111280.

[45] Y. Chen and C. F. Wang, "Characteristic-mode-based improvement of circularly polarized U-slot and E-shaped patch antennas," *IEEE Antennas Wireless Propag. Lett.*, vol. 11, pp. 1474–1477, Nov. 2012, doi: 10.1109/LAWP.2012.2231046.

[46] F. A. Dicandia and S. Genovesi, "Linear-to-circular polarization transmission converter exploiting meandered metallic slots," *IEEE Antennas Wireless Propag. Lett.*, vol. 21, no. 11, pp. 2191–2195, Nov. 2022, doi: 10.1109/LAWP.2022.3188063.

[47] W. Tang, G. Goussetis, N. J. G. Fonseca, H. Legay, E. Sáenz, and P. de Maagt, "Coupled split-ring resonator circular polarization selective surface," *IEEE Trans. Antennas Propag.*, vol. 65, no. 9, pp. 4664–4675, Sep. 2017, doi: 10.1109/TAP.2017.2726678.

[48] I. Lopez and J.-J. Laurin, "A circular polarization selective surface implemented on a flexible substrate," *IEEE Trans. Antennas Propag.*, vol. 62, no. 7, pp. 3847–3852, Jul. 2014, doi: 10.1109/TAP.2014.2318777.

[49] A. Ericsson and D. Sjöberg, "Design and analysis of a multilayer meander line circular polarization selective structure," *IEEE Trans. Antennas Propag.*, vol. 65, no. 8, pp. 4089–4101, Aug. 2017, doi: 10.1109/TAP.2017.2710207.

[50] E. Safin and D. Manteuffel, "Reconstruction of the characteristic modes on an antenna based on the radiated far field," *IEEE Trans. Antennas Propag.*, vol. 61, no. 6, pp. 2964–2971, Jun. 2013, doi: 10.1109/TAP.2013.2251312.

[51] R. Singh, I. Al-Naib, W. Cao, C. Rockstuhl, M. Koch, and W. Zhang, "The Fano resonance in symmetry broken terahertz metamaterials," *IEEE Trans. THz Sci. Technol.*, vol. 3, no. 6, pp. 820–826, Nov. 2013, doi: 10.1109/TTHZ.2013.2285498.

[52] M. Wang et al., "Tunable Fano resonance and plasmon–exciton coupling in single au nanotriangles on monolayer WS$_2$ at room temperature," *Adv. Mater.*, vol. 30, no. 22, May 2018, Art. no. 1705779, doi: 10.1002/adma.201705779.

[53] S. M. A. M. H. Abadi and N. Behdad, "Wideband linear-to-circular polarization converters based on miniaturized-element frequency selective surfaces," *IEEE Trans. Antennas Propag.*, vol. 64, no. 2, pp. 525–534, Feb. 2016, doi: 10.1109/TAP.2015.2504999.

[54] J. Sanz-Fernández, E. Saenz, and P. de Maagt, "A circular polarization selective surface for space applications," *IEEE Trans. Antenna Propag.*, vol. 63, no. 6, pp. 2460–2470, Jun. 2015, doi: 10.1109/TAP.2015.2414450.

**Francesco Alessio Dicandia** (Member, IEEE) was born in Carrara, Italy, in 1988. He received the bachelor's and master's degrees in telecommunications engineering and the Ph.D. degree in information engineering from the University of Pisa, Pisa, Italy, in 2012, 2014, and 2018, respectively.

From November 2017 to August 2020, he worked with Greenwaves srl, Milan, Italy, as a Microwave/Antenna Engineer within which he was responsible for several industrial antenna development and projects in the field of 5G systems. From September 2020 to October 2022, he worked with IDS Ingegneria dei Sistemi, Pisa, within the Electromagnetic Engineering Division. Since November 2022, he has been a Researcher with the National Research Council (CNR), Institute of Electronics, Information Engineering and Telecommunications (IEIIT), Pisa. His research activity is mainly focused on characteristic modes analysis, reconfigurable antennas, multiple-input-multiple-output antennas, phased arrays, and radio frequency identification systems.

Dr. Dicandia was a recipient of the Three-Years Grant provided by the Consorzio Nazionale Interuniversitario per le Telecomunicazioni (CNIT), Pisa, in 2014.

**Simone Genovesi** (Senior Member, IEEE) received the Laurea degree in telecommunication engineering and the Ph.D. degree in information engineering from the University of Pisa, Pisa, Italy, in 2003 and 2007, respectively.

Since 2003, he has been collaborating with the Electromagnetic Communication Laboratory, Pennsylvania State University (Penn State), University Park, PA, USA. From 2004 to 2006, he was a Research Associate with the ISTI Institute, National Research Council of Italy (ISTI-CNR), Pisa. From 2015 to 2017, he was several times a short-term Visiting Researcher with the Grenoble Institute of Technology, Valence, France, and Universitat Rovira I Virgili, Tarragona, Spain. He is currently an Associate Professor with the Dipartimento di Ingegneria dell'Informazione, University of Pisa. He is also the Coordinator of the Additive Manufacturing founded in the framework of the Departments of Excellence ("Dipartimenti di Eccellenza") funded by the Italian Ministry of Education, University and Research. His current research topics focus on additive manufacturing, sensors, radio frequency identification (RFID) systems, and reconfigurable antennas.

Dr. Genovesi is also an Associate Editor of the IEEE TRANSACTIONS ON ANTENNAS AND PROPAGATION.